NJC

Accepted Manuscript

Volume 40 | Number 1 | January 2016 | Pages 1–846

NJC

New Journal of Chemistry
www.rsc.org/njc

A journal for new directions in chemistry

ISSN 1144-0546

ROYAL SOCIETY OF CHEMISTRY

PAPER
Jason B. Benedict et al
The role of atropisomers on the photo-reactivity and fatigue of diarylethene-based metal–organic frameworks

cnrs

This is an Accepted Manuscript, which has been through the Royal Society of Chemistry peer review process and has been accepted for publication.

Accepted Manuscripts are published online shortly after acceptance, before technical editing, formatting and proof reading. Using this free service, authors can make their results available to the community, in citable form, before we publish the edited article. We will replace this Accepted Manuscript with the edited and formatted Advance Article as soon as it is available.

You can find more information about Accepted Manuscripts in the author guidelines.

Please note that technical editing may introduce minor changes to the text and/or graphics, which may alter content. The journal's standard Terms & Conditions and the ethical guidelines, outlined in our author and reviewer resource centre, still apply. In no event shall the Royal Society of Chemistry be held responsible for any errors or omissions in this Accepted Manuscript or any consequences arising from the use of any information it contains.

ROYAL SOCIETY OF CHEMISTRY

Journal Name

ARTICLE

Synthesis process, size and composition effects of spherical Fe₃O₄ and FeO@Fe₃O₄ core/shell nanoparticles

Pablo Tancredi[a],*, Patricia C. Rivas Rojas[a], Oscar Moscoso-Londoño[b,c], Ulrike Wolff[d], Volker Neu[d], Christine Damm[d], Bernd Rellinghaus[d], Marcelo Knobel[b] and Leandro M. Socolovsky[a]

In this work we investigate the size, composition and magnetic behavior of a series of iron oxide nanoparticles prepared by means of high temperature decomposition of an iron oleate precursor. Different synthesis conditions, as gas atmosphere, precursor's ratio and heating rate were tested to obtain a direct correlation between the final sample structure and the varied parameter. The synthesis products were characterized by X-ray diffraction, transmission electron microscopy and small angle X-ray scattering, respectively. We studied six samples, with rather narrow size distribution and mean diameters from 8 nm to 16 nm. The particles with diameter below 11 nm were found to be spinel-type, monocrystalline, and their magnetic response can be ascribed to a single-domain framework. On the other hand, two-phase core-shell FeO@Fe₃O₄ of mean size of 15 nm and 16 were obtained by increasing the amount of oleic acid and the heating rate. The magnetic behavior of these samples exhibits interesting interface features, related to the exchange coupling phenomenon between the FeO and Fe₃O₄. We discuss how the different synthesis conditions may lead to the presence of this FeO phase, and how the core-shell configuration and other structural features affect the macroscopic magnetic behavior.

1. Introduction

The unique magnetic properties of iron oxide nanoparticles (IONPs) make them one of the most investigated nanomaterials[1,2]. In the last years, these systems were studied and already exploited in several technological applications, such as chemical sensors[3], recording media devices, magnetic ferrofluids employed in sealing, as well as many biomedical uses such as biomolecule separation, drug targeting, magnetic hyperthermia, contrast agents for nuclear magnetic resonance images, among others[4,5].

The nanoparticles properties and performance depends on the system's chemical and physical characteristics, which are strongly determined by the synthesis method employed in their preparation[6-8]. In particular, the magnetic behavior is known to be related to various structural features, like the mean particle size, the size distribution, the agglomeration state, the crystallinity and the iron oxide crystalline phases[9-11].

Among the diverse methods to prepare IONPs, the thermal decomposition of iron oleate precursors has been very well described and extensively used in the last decade since its first description[12]. This method allows the preparation of large quantities of IONPs, with good tuning of the average size and size distribution. According to some authors, the nanoparticles are produced by a classical nucleation followed by a delayed growth process, with the two stages separated by the temperature at which each one take places[12-14]. The IONPs prepared by this method turn out to become non-aggregated and highly crystalline, so one can easily link the macroscopic magnetic behavior of a system of nanoparticles to its structure at the nanoscale.

The classical thermal decomposition employing iron (III) oleate as precursor results in the production of spinel-type iron oxides, magnetite (Fe₃O₄) or/and maghemite (γ-Fe₂O₃) as the only constituents[12-15]. These particles are single domain systems, and behave as typical superparamagnets at room temperature. In the last years, some authors managed to produce particles with a core/shell structure of wüstite/magnetite phases (FeO/Fe₃O₄)[16-19]. Core/shell structures have been extensively studied for cubic-shaped IONPs obtained by the decomposition of iron oleate with sodium oleate instead of oleic acid. In these systems, the change of the stabilization agent not only directs the crystal growth towards the cubic-shape, but also boosts the conversion of Fe^{3+} to Fe^{2+} to produce the more reduced FeO phase[17,19]. In addition, some reports have succeeded in synthesizing spherical core/shell nanoparticles with oleic acid as surfactant, but they do not mention the key reaction conditions that lead to the formation of these structures instead of the full-spinel system[20-24].

a. Laboratorio de Sólidos Amorfos, Instituto de Tecnologías y Ciencias de la Ingeniería "Hilario Fernández Long", Facultad de Ingeniería, Universidad de Buenos Aires – CONICET, Buenos Aires, Argentina. Email: pablotancredi@gmail.com
b. Laboratório de Materiais e Baixas Temperaturas, Instituto de Física 'Gleb Wataghin', Universidade Estadual de Campinas, Campinas, Brazil.
c. Universidad Autónoma de Manizales, Antigua Estación del Ferrocarril, Manizales, Colombia.
d. IFW Dresden, Leibniz Institute for Solid State and Materials Research Dresden, Helmholtzstrasse 20, 01069, Dresden, Germany.

Core/shell nanostructures with two different magnetic phases present some interesting features related to the coexistence, in a single entity, of two crystalline phases with distinctive magnetic behavior. For instance, FeO has an antiferromagnet (AFM) behavior below the Néel temperature (T_N), approximately at 200 K, while the spinel iron oxides Fe_3O_4 and $\gamma\text{-}Fe_2O_3$ display a ferrimagnetic order (F(i)M). The existence of the AFM/F(i)M interface in the nanoparticles leads to an exchange coupling phenomenon[25], that can result in the enhancement of the coercive field and/or the presence of an exchange bias phenomena, *i.e.*, a horizontal shift of the hysteresis loop after field cooling of the material. This kind of behavior has been described in many iron containing nanoparticles, such as $CoO/CoFe_2O_4$[26], $CoFe_2O_4/\gamma\text{-}Fe_2O_3$ and $MnFe_2O_4/\gamma\text{-}Fe_2O_3$[27] core/shell nanoparticles, as well as Au/Fe_3O_4 dumbbell-shaped nanoparticles[28,29]. In particular, the performance of exchange coupled nanoparticles can be attractive for applications related to spintronics and magnetic recording, since the coercivity enhancement helps to overcome the superparamagnetic limit[19,25]. Also, it was recently reported that FeO/Fe_3O_4 core/shell structures have a more efficient heat induction capacity and a better performance for magnetic hyperthermia therapies, without compromising the surface related properties because the exposed phase is still magnetite as in the typical single-phase systems.[30]

In this work, by an accurate control of the amount of stabilization agent, the heating rate and the gas reaction atmosphere in the thermal decomposition synthesis process we managed to produce a set of IONPs samples with a distinct occurrence of two iron oxide phases, wüstite (FeO) and magnetite (Fe_3O_4). All samples were obtained directly from the synthesis with no further treatment. In particular, we have focused in the synthesis conditions that can lead to the emergence of the wüstite phase and we have advanced towards understanding how they affect the final nanoparticle structure and the magnetic behavior of the system.

2. Experimental

2.1 Materials

The chemicals employed in this work were, iron (III) chloride hexahidrate ($FeCl_3 \cdot 6H_2O$, 97%, Tetrahedron), sodium hydroxide (NaOH, 99%, Anedra), oleic acid (technical grade, 90%, Sigma-Aldrich), 1-Octadecene (technical grade, 90%, Sigma-Aldrich). All chemicals were used as received without further purification.

2.2 Methods

A series of hydrophobic IONPs were prepared by thermal decomposition of an iron organometallic precursor, according to literature[12].

Synthesis of iron oleate: 2 mmol of iron oleate, $Fe(oleate)_3$, was prepared by mixing 2 mmol of $FeCl_3 \cdot 6 H_2O$, 6 mL of water, 8 mL of ethanol, 14 mL of hexane and 1.9 mL of oleic acid. Upon the addition of 0.24 g of NaOH, $Fe(oleate)_3$ begins to form and migrates to the organic layer. The temperature was set at 60°C and the system was stirred for 3 hours. Finally, the organic layer was collected, washed three times with deionized water and heated gently overnight to obtain a brown-sticky precursor of $Fe(oleate)_3$.

Synthesis of IONPs: The $Fe(oleate)_3$ precursor was dissolved in 15 mL of 1-octadecene and a variable amount of oleic acid. The solution was maintained at 125°C for 1 h, and then heated at 320°C with variable heating rates. Then, the mixture was cooled to room temperature and IONPs were precipitated and isolated by the addition of 45 mL of acetone/$CHCl_3$ (1:3) and centrifugation at 3500 RPM for 30 minutes. The isolated solid was washed 3 times with a acetone/$CHCl_3$ mixture to finally being redispersed in hexane.

A scheme of the synthesis conditions employed in this work is presented in Table 1.

2.3 Characterization

Structural characterization was carried out via X-ray diffraction (XRD) in a commercial diffractometer with standard Cu K-alpha radiation, and with small-angle X-ray scattering (SAXS), measured at the SAXS line (National Synchrotron Light Laboratory, LNLS-CNPEM, Campinas, Brazil). The measured SAXS patterns were analyzed with SasView software. Morphology and size distribution of the samples have been obtained by transmission electron microscopy (TEM), with a FEI-Tecnai microscope at the Leibniz Institute for Solid State and Materials Research (IFW Dresden, Germany). The magnetic properties of the prepared samples were evaluated by the hysteresis loops at several temperatures between 5 and 300 K as well as zero field cooling and field cooling curves (ZFC/FC) using a MPMS XL Quantum Design SQUID magnetometer.

Table 1: Reaction conditions employed in the sample synthesis

Sample	Iron oleate (mmol)	Oleic acid (mmol)	Heating rate (°C/min)	Gas atmosphere
S1	2	2	4	Ar
S2	2	2	4	Air
S3	2	1	4	Ar
S4	2	1	4	Air
S5	2	2	2	Ar
S6	2	1	2	Ar

3. Results and discussion

3.1 Structural and morphological studies

The six prepared samples are non-aggregated, stable hydrophobic suspensions that strongly respond to the presence of an external magnetic field.

X-ray diffraction was performed on the dried samples to identify the crystalline phases present in the IONPs. Figure 1 shows the obtained diffractograms of samples S1, S2, S3 and S6. Although the syntheses were carried out in a similar way, clear differences in the X-ray diffraction patterns are observed. For example, samples S3 and S6 exhibit a single diffraction contribution that corresponds to the iron oxide of the inverse spinel structure (Fe_3O_4, magnetite

Journal Name

ARTICLE
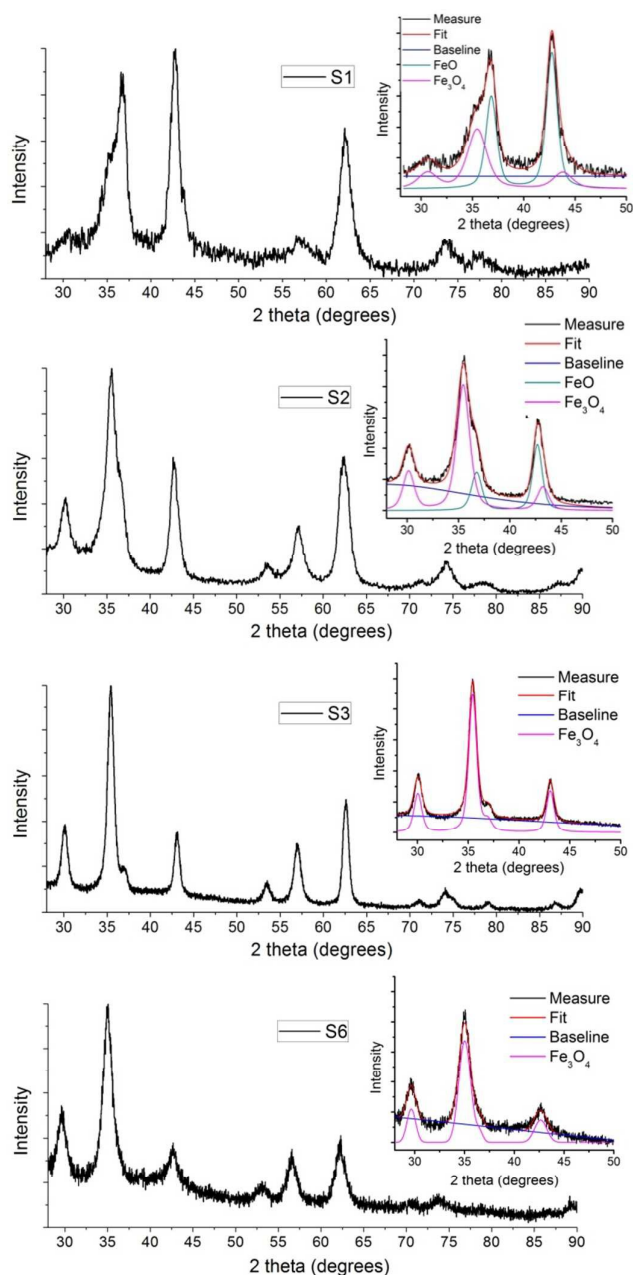
Figure 1. X-Ray Diffraction patterns of samples S1, S2, S3 and S6. Inset: fast deconvolution of the data from 25° – 50° to illustrate the contribution of the different phases.

or/and γ-Fe$_2$O$_3$, maghemite). Also, a single phase XRD diffractogram was obtained for samples S4 and S5 (not shown here). The crystallite sizes, calculated by the Scherrer equation from the peak at 2θ ≈ 35° (family of [311] planes), were ~9.6 nm, ~10.4 nm, ~9.4 nm and ~6.3 nm for samples S3, S4, S5 and S6 respectively. On the other hand, samples S1 and S2 diffractograms show two major contributions, one that corresponds to the same spinel structure as S3 and S6, and the other that corresponds to FeO (wüstite) crystalline phase. Furthermore, there is a clear difference in the relative contribution of the FeO phase in these samples, indicating

that the relative amount of FeO is larger for S1 than for S2. Figure 1 also shows the deconvolution of the diffractograms between 25° and 50°, performed to highlight these differences. Expected relative heights and full width at half maximum were preserved for peaks of the same phase. Due to the similarities of the XRD spectra of samples S4 and S5 with other prepared samples, we focus the attention to examine the main results obtained from the samples S1, S2, S3 and S6, respectively.

Figure 2 shows the TEM images of the IONPs of samples S1, S2, S3 and S6, respectively. Nearly spherical shape systems with a narrow particle size distribution can be seen in all samples. From several TEM images a mean size for each sample were obtained, leading to ~16.0 nm, ~15.5 nm, ~10.6 nm and ~7.7 nm for S1, S2, S3 and S6, respectively. In sample S1, some particles show a clear contrast between the core and an outer layer, a possible evidence of a core/shell structure formed by distinct phases present in the particle. HR-TEM was performed on samples S1 and S3 to visualize the crystalline structure of the selected particles. For instance, the HR-TEM micrograph of sample S3 (figure 2.B) shows clearly a monocrystalline nanoparticle, in accordance with the single-phase system identified in the X-ray diffractogram. For sample S1 (figure 2.A), the HR-TEM micrograph shows a crystalline outer layer formed by several planes and what seems to be an amorphous core, with no clear crystalline arrangement. This evidence suggests the coexistence of different crystallites and phase components in the same particle.

Besides the crystalline structure variances revealed in the X-ray diffraction patterns, the reaction conditions employed in the synthesis route also lead to some differences in the size distributions of the IONPs, as can be seen from the TEM images. For example, IONPs from sample S3 are a few nanometers smaller than those from samples S1 and S2. This difference is related to the well documented tendency that links the decrease of the ratio of iron oleate / oleic acid with the increase in size of the IONPs[31]. This trend is usually exploited to produce series of IONPs of pure spinel phase. However, it seems that above a certain ratio of oleic acid / iron oleate, the iron species in the reaction system experience an over-reductive environment and larger nanoparticles are formed with a wüstite component. The existence of the reduced iron oxide phase in nanoparticles larger than 15 nm when employing high amounts of oleic acid was observed in several works. Nanoparticles of samples S1 and S2 have similar size distribution but, as X-ray analysis revealed, they differ in the crystalline relative composition. The similar size can be a consequence of the same amount of oleic acid employed, while the crystalline composition difference can be related to the argon atmosphere employed in S1 synthesis, but not in the synthesis of S2. The reductive conditions needed to produce the FeO phase are generated by the decomposition of the organic precursors at high temperatures. This reaction produces species like CO, which can reduce Fe^{3+} atoms to Fe^{2+} atoms. In sample S1, the Ar atmosphere at the beginning of the thermal decomposition enhances the reductive conditions by eliminating O$_2$ from the system, as this molecule can also act as an electron acceptor instead of the Fe atoms. Thus, the reaction carried out with Ar

ARTICLE

Journal Name

atmosphere produces IONPs with a bigger shield of FeO. Strikingly,
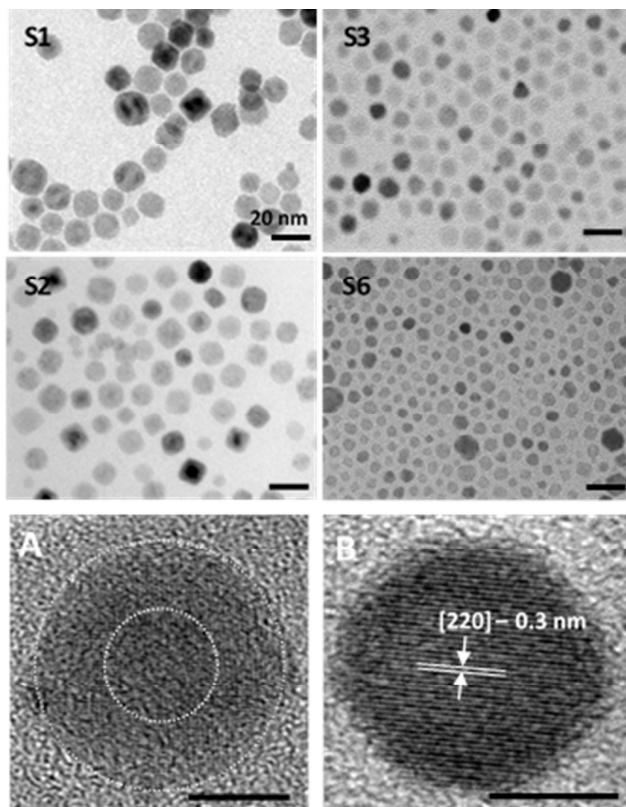
Figure 2: TEM images of the studied nanoparticles. The mean diameters are 16.0 nm for S1, 15.5 nm for S2, 10.6 nm for S3 and 7.7 nm for S6. HR-TEM of a core-shell nanoparticle from sample S1 (A) and a single-crystal nanoparticle from sample S3 (B). Scale bar is 5 nm for both HR-TEM images.

no big differences in the crystalline phases and crystallite grain sizes were observed in the synthesis carried out with and without Ar atmosphere for a lower iron oleate / oleic acid ratio (sample S3 was prepared with Ar, sample S4 was prepared in air).

The heating rate during the IONPs synthesis was also studied. Samples S5 and S6 were prepared with the same reaction conditions employed in S1 and S3, respectively, but with a heating rate of 2 °C/min instead of 4 °C/min. The products of these syntheses are nanoparticles of pure-spinel phase, a few nanometers smaller than the ones obtained with the faster heating rates. The observed relationship that links a slower heating rate with the formation of smaller nanoparticles was also perceived before, and has been discussed by other authors[32].

In summary, the results discussed above suggest that the emergence of the reduced FeO phase is not an exclusive effect of the reductive conditions generated in the reaction, but it is also linked to the IONPs size by the ratio of oleic acid / iron oleate and the heating rate employed in the synthesis. The used synthesis protocol and the structural characterization of the core/shell FeO/Fe_3O_4 samples suggests that the reduced phase is produced during the development of the IONPs, and not as a further transformation once the IONPs are fully formed. In this

configuration, once the reductive environment is gone, the FeO phase at the core is protected from phase conversion (e.g. oxidation to magnetite) by the spinel phase at the outside layer, so the core/shell structure can stand virtually unchanged for long time periods and mild redox conditions.

A possible explanation of the behavior observed for the synthesis products was proposed by Lak et al[23]. At first, the de-attachment of oleate ligands in the iron complexes can lead to small FeO crystallites. The CO released by precursor decomposition at this instance generates the reductive conditions and may be responsible for the Fe^{3+} to Fe^{2+} conversion. As the nanoparticle grows, Fe^{2+} atoms are transported to the developing surface and tend to oxidate to Fe^{3+} to form magnetite, a thermodynamically most stable iron oxide phase. Here, the diffusion length of this transport seems to define the possibilities of phase coexistence. For smaller IONPs like those presented in samples S3 and S6, a complete oxidation to magnetite may occur during the synthesis and in the washing steps. In addition, a slower heating rate favors this conversion by extending the reaction time and, consequently, the oxidation process at the surface. On the other hand, for larger particles, the existence of a longer diffusion path hampers the oxidation process and a significant fraction of FeO can remain intact at the center, leading to the formation of the core/shell structure. Despite a single report with a core/shell structure with diameter under 10 nm[22], this approach explains why it is so difficult to obtain IONPs smaller than 12 nm with core/shell morphology, even employing Ar atmosphere. If it is necessary, on a post-synthesis process the FeO phase can be easily oxidized to form a single-phase Fe_3O_4 or γ-Fe_2O_3 nanoparticle by O_2 thermal assisted oxidation[15,17].

SAXS measurements were performed on the hexane dispersions of three selected samples S2, S3 and S6. The purpose was to compare the scattering profiles and the fitting results for and to correlate it with the information extracted from the TEM analysis. The scattering intensity ($I(q)$) vs. scattering vector (q) plotted in the double logarithmic representation are presented in Figure 3 (a). For these three samples, the scattering intensity displays typical features of well dispersed nanoparticles; *i.e.*, at low q-regions the system better follows closely a Guinier behavior indicating negligible aggregation, while for intermediate q-values a smooth oscillatory behavior is observed, indicating a particle finite size distribution with low polydispersity. At this region, some differences can be recognized; for example, the first intensity drop occurs at a smaller q value in sample S2 than for sample S3, as well as in sample S3 with respect to sample S6, This tendency reveals the differences in the mean size of the scattering objects and in nanoparticle size distribution broadness. Furthermore, for higher q-values, the expected Porod behavior ($I(q) \sim q^{-4}$) is masked by an incoherent background. Such behavior comes from the dissolution of oleic acid molecules in the hexane solution and also can be attributed to the presence of oleic acid molecules bound to the surface of the nanoparticles[33]. The experimental scattering intensity of a set of nano-objects can be represented by:

Please do not adjust margins

Journal Name   ARTICLE

$$I(q) = K \cdot P(q) + Bkg \qquad (1)$$

where K is a scale factor that associates the scattering-length difference between the nanoparticles and the IONPs, $P(q)$ is a form factor regarding information on the shape of the scatterers. A q-independent term was added to consider the incoherent background scattering (Bkg). The sample holder and the hexane contributions were corrected by subtracting their respective scattering signals. Then, the form factor of a set of diluted spherical particles is given by:

$$P(q) = \int_0^\infty \frac{3V(\Delta\rho)(sen(qr) - qr\cos(qr))^2}{(qr)^3} f(r)dr \qquad (2)$$

Here r is the nanoparticle radius, V the nanoparticle volume and $f(r)$ is the size distribution of particles with mean radius r_0. According to the TEM information, $f(r)$ was assumed as Gaussian-type.

Using eq. 1 and the form factor for diluted spherical particles (eq. 2), the SAXS intensities were well fitted (presented as solid lines in figure 3(a)). From these fits relevant structural parameters where obtained, such as the mean radius r_0 (related to the mean diameter through $D_{SAXS} = 2r_0$) and the standard deviation (σ). For sample S3, the best fitting results indicate a mean diameter of 12.0 nm with σ = 1.4 nm. For sample S6, the mean diameter is 8.8 nm with σ = 1.0 nm. The procedure to fit the SAXS intensities of sample S2 was briefly modified, this time a second form factor, also of spherical diluted particles, was added in order to take into account a second population of particles with mean radius $r_{0,2}$. Then, the scattering intensity of this sample was fitted by:

$$I(q) = K_1 \cdot P_1(q) + K_2 \cdot P_2(q) + Bkg \qquad (3)$$

Here, the first and the second terms represent the two families of scattering objects, each one with a different mean radius. Following eq. 3 to fit the SAXS data of sample S2, a main family of particles of mean diameter 15.8 nm with standard deviation of 1.6 nm was obtained. According to our calculation, this set of scattering particles represents approximately the 97% of the sample. For the second population of particles, a mean diameter of 1.0 nm with standard deviation of 0.5 nm was obtained. The presence of this second ensemble of smaller nanoparticles could be the result of a redissolution during the synthesis process of some larger particles. Despite the sample S2 contains the two iron oxide phases, the slight difference in electron density between them hinders the possibility to distinguish from core-shell or any other structure that could have formed during the synthesis. For all studied samples the SAXS diameter values are slightly higher but in good agreement with those derived from TEM analysis and obtained by the Scherrer equation. The best fit parameters are summarized in Table 2.

Table 2: Nanoparticle sizes derived from the XRD, TEM and SAXS analysis

Sample	D_{XRD} (nm)	D_{TEM} (nm)	D_{SAXS} (nm)	Presence of FeO
S1	----*	16.0	----	Yes
S2	----*	15.5	15.8	Yes
S3	9.6	10.6	12.0	No
S4	10.4	11.0	----	No
S5	9.4	10.7	----	No
S6	6.3	7.7	8.8	No

*D_{RXD} was not calculated due to the overlapping of the principal peaks associated to the FeO and Fe_3O_4 phases

3.2 Magnetic Properties
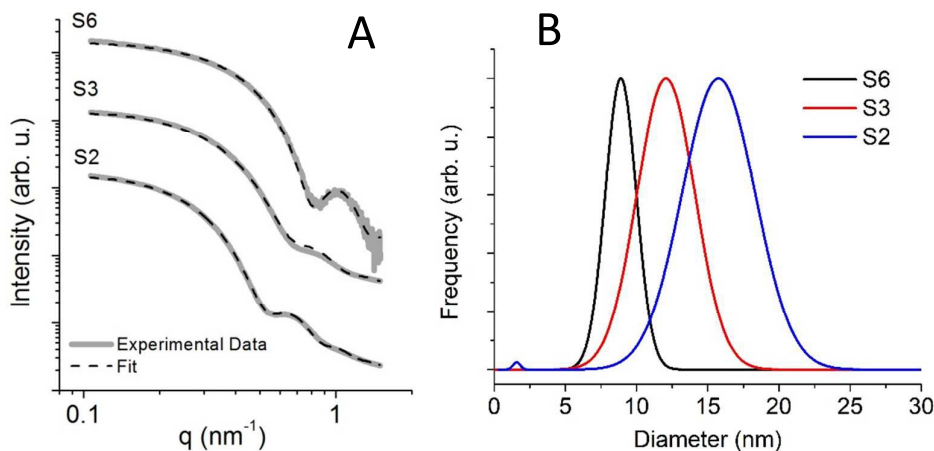
Figure 3. (A) SAXS intensities plotted in a double logarithmic representation for three of the studied samples. Fitted curves are represented as a grey continuous line. (B) SAXS Gaussian diameter distribution of the nanoparticles obtained from the fitted curves

ARTICLE
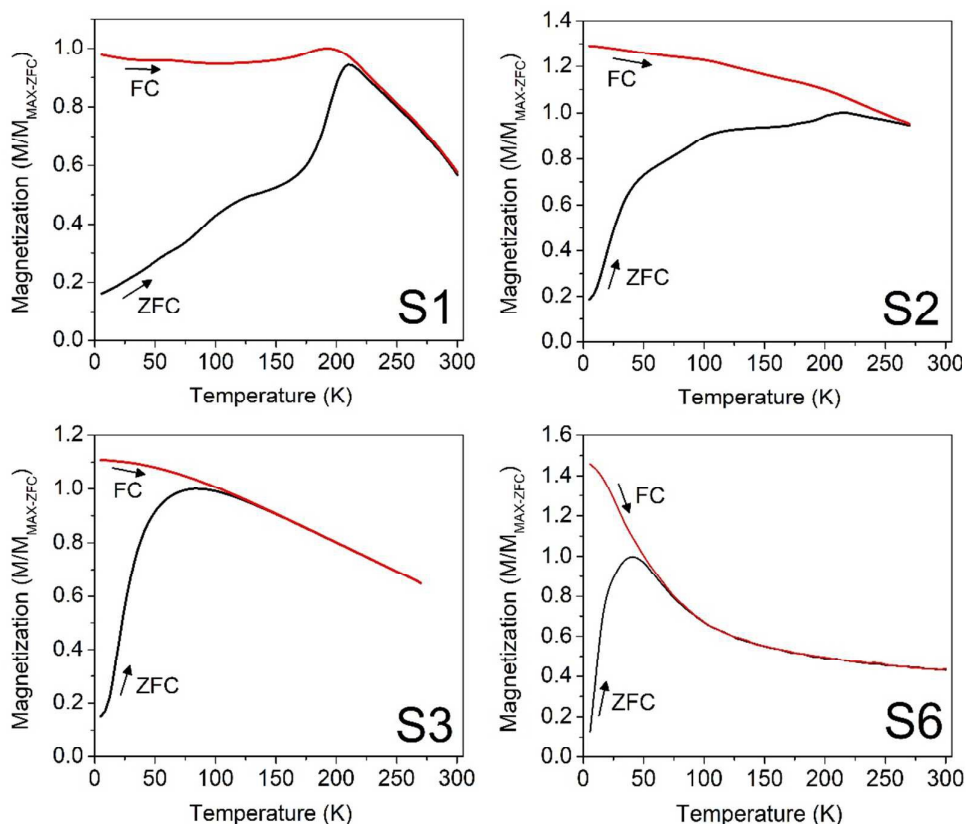
Figure 4. Normalized zero field cooling (ZFC) and field cooling (FC) curves for samples S1, S2, S3 and S6. All of the curves were recorded with an applied magnetic field of 100 Oe.

In the previous section we presented and discussed the structural features of the synthesized samples, emphasizing in the coexistence of distinct iron oxide phases and how the synthesis conditions define the morphology and the phase compositions. Magnetic properties of a nanop articulate system are strongly related to the system's structural features, especially if different crystalline phases are present. Moreover, the nanoscale dimensions of the structures reveal additional magnetic phenomena which need to be considered to understand the behavior of the systems.

The magnetization temperature dependence of the studied samples was recorded in the zero-field-cooling (ZFC) and field-cooling (FC) modes with an applied magnetic field set to 100 Oe. As it can be seen in figure 4, clear differences in the magnetic response of the samples were measured, which can be linked to structural dissimilarities between the nanoparticles systems[2,34].

Samples S3 and S6 show the typical behavior of weakly or non-interacting single domain nanoparticles that are blocked at low temperatures and in the superparamagnetic regime at temperatures approximately above the ZFC peak (T_{MAX}). These peaks are clearly distinguished and their values change from one sample to another, being $T_{MAX} \approx 100$ K and 45 K for samples S3 and S6, respectively. Such temperature is related to the so-called

blocking temperature (T_B), which identifies the temperature of the transition between the blocked and the superparamagnetic regimes[2,34,35]. Comparable ZFC maximum values have been reported for Fe_3O_4 diluted nanoparticles of nearly similar size[15,31].

The irreversibility temperature (T_I) is defined as the temperature where the ZFC curve bifurcate from the FC curve, and it is related to the blocking temperature distribution (which, in turn, is a direct consequence of the size distribution)[2,34,35]. For sample S3 it was $T_I = 125$ K, while for sample S6 it was $T_I = 75$ K. The relatively small difference between T_{MAX} and T_I confirms a very narrow blocking temperature distribution.

For spherical and single domain nanoparticles, the net magnetic moment can be represented with a classical vector whose magnitude, under the simplest assumption, can be expressed as $\mu = \mu_{AT} N$, where μ_{AT} is the atomic magnetic moment and N being the number of magnetic atoms[2]. For temperature ranges of $T > T_B$, the net magnetic moment can fluctuate between two equilibrium states, which are defined by the easy axes. For this temperature ranges, the magnetization can be modelled by an Arrhenius-type law. In the absence of thermal fluctuations (low temperatures, typically for $T < T_B$), the energy required for the spin to flip is the

energy necessary to overcome the magnetic anisotropy barrier (E_A), given by the following equation:

$$E_A = -K_U V_i \left(\frac{\vec{\mu}_i \cdot \vec{n}_i}{|\vec{\mu}_i|}\right)^2 \qquad (4)$$

where K_U is the uniaxial anisotropy constant, V_i the volume of the particle i, and $\vec{n}_i$ is the direction of the easy axis of the particle i.

For well diluted dispersions of magnetic nanoparticles, where dipole-dipole interactions can be neglected, the thermal energy ($k_B T$) of the system defines the dominant magnetic state. When $k_B T$ becomes bigger than E_A, the rotation barrier is overcome and the giant magnetic moment fluctuates around the easy axis. At this condition the nanoparticles are in the so-called superparamagnetic regime because the time average of magnetic moment fluctuation is shorter than the typical magnetization length. On the other hand, when the thermal energy is insufficient to cause a reversal of the spin on the measurement time scale, the magnetic moment is fixed along one direction of the easy axis and the nanoparticles are in the blocked state[2].

In a simplified approach, the differences in the T_{MAX} values for samples S3 and S6 can be directly related to the size of the nanoparticles. As the size of the particles increase, so does the energy of the magnetic anisotropy barrier, E_A. Therefore, the temperature where the product $k_B T$ overcomes E_A, i.e. the temperature of the transition between the blocked and the superparamagnetic state, needs to be higher for particles of larger size.

The nearly ideal single domain behavior of samples S3 and S6 is directly linked to the single crystalline structure of the nanoparticles. Because Fe_3O_4 is the only iron oxide phase, the magnetization can be well represented by a giant magnetic moment along the whole nanoparticle volume, an indication that no strong interface effects are present and the magnetization can be well described by the well-known superparamagnetic theory.

For samples S1 and S2 (FeO/Fe_3O_4 systems) a more complex temperature magnetization dependence takes place. For instance, a sharp peak at 200 K can be observed in sample S1. This peak indicates the transition from the antiferromagnetic to the paramagnetic state of the FeO phase, and is defined by the Néel temperature (T_N). The same transition is seen in sample S2, but the sharpness of the peak is notoriously diminished. This difference is a direct consequence of the larger yield of FeO in sample S1 when compared with sample S2[23]. Also, between both samples the position of the Néel temperature practically remains the same point, suggesting that the FeO Neel transition is independent of the crystalline grain size. At temperatures below 200 K some other phenomena can be considered in both cases. For sample S1, the shoulder in the ZFC curve observed near 125 K can be a consequence of the blocked-to-superparamagnetic transition of the Fe_3O_4 phase of the IONPs, while for sample S2 two clearly differentiated shoulders at 50 K and 125 K are observed in the ZFC
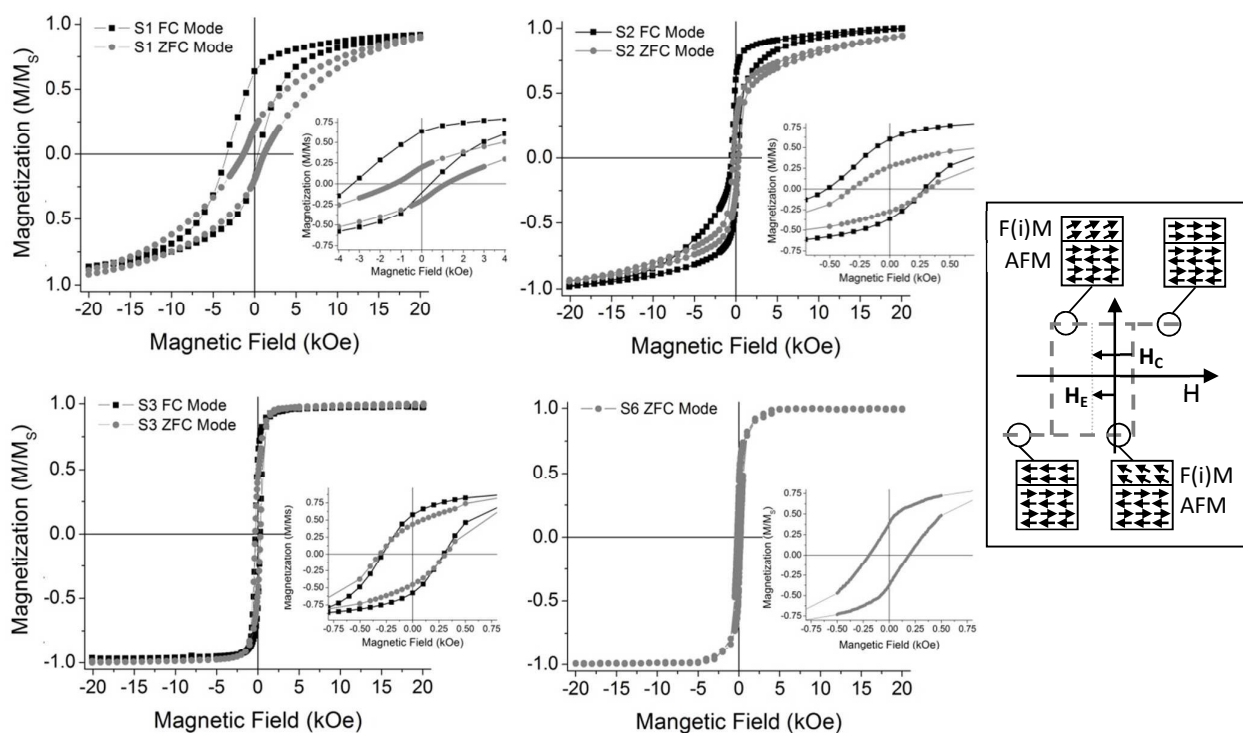
Figure 5: Magnetization vs. applied magnetic field curves at T = 5 K recorded in zero field cooling (ZFC) and field cooling (FC) modes. The M vs. H curves measured in the FC mode were obtained cooling down the sample with H = 2 kOe. All curves are normalized to the saturation magnetization. Inset: zoom at low fields showing the coercive and exchange bias fields. Right: Scheme of the exchange bias field formation in the FC measurement.

New Journal of Chemistry Accepted Manuscript

curve. We understand these steps as two different unblocking events, one that corresponds to Fe_3O_4 in core-shell nanoparticles and the other to single-phase Fe_3O_4 nanoparticles. The IONPs formation and reaction process suggested previously and the low yield of FeO evidenced by XRD in this sample could lead to a system composed of both core/shell and single-phase nanoparticles. Oxidation during synthesis and further sample manipulation could have not been completely homogeneous, and some particles may have oxidized to a single-phase state while the majority is still in a core/shell configuration, giving the discrete two events observed in the magnetic measurement. Finally, the one shoulder in sample S1 can be due to the large FeO yield that prevents the formation of single-phase Fe_3O_4 nanoparticles.

The exchange coupling effect at the AFM/F(i)M interface in the FeO/Fe_3O_4 nanoparticles was investigated by means of M vs. H measurements recorded at low temperatures cooling the sample with and without an external magnetic field. The measurements were performed at 5 K, after cooling in the absence of an applied magnetic field (ZFC), and with an applied magnetic field of 2 kOe (FC). This temperature is far below the Néel temperature of FeO and from the blocking events of the superparamagnetic phase.

On both single-phase systems (samples S3 and S6), the saturation magnetization (M_S) obtained at 5 K is practically identical to those values reported for pure Fe_3O_4 nanocrystals (≈80 emu/g). For FeO/Fe_3O_4 IONPs, the presence of the FeO phase results in a saturation magnetization fall, an expected result due to the low contribution to the magnetization of the antiferromagnetic component. For instance, the measured M_S value at 5 K for the sample S1 is almost half the one of samples S3 and S6.

The M vs. H dependence for sample S3 reveals no major differences between ZFC and FC measurement modes (figure 5), with no horizontal shift of the loop and a coercive field (H_C) of ~290 Oe in both cases. Again, this behavior is the consequence of the single-phase ferrimagnetic crystalline system, and confirms the conclusions drawn from previous characterizations. On the contrary, a notorious difference between both modes appears for samples S1 and S2. Some main discrepancies can be analyzed in the context of the AFM/F(i)M core/shell structure suggested by previous characterizations.

At room temperature, the FeO phase has a paramagnetic spin configuration, and after cooling down this sample to 5 K (below T_N of FeO) under an applied field, the spins orient in an antiferromagnetic way. At this temperature, the uncompensated spins of FeO at the interface are pinned with the Fe_3O_4 spins in a parallel alignment. During the magnetic field loop, the magnetic anisotropy of the AFM component is high enough to fix the interfacial spins and induce the negatively shifted hysteresis loop, as described by the scheme in figure 5. The loop shift (obtained at FC conditions) is numerically defined by the exchange bias field, H_E. The difference in the magnitude of H_E for samples S1 and S2 can be ascribed to the larger yield of FeO that enhances the interface area and so the pinning effect in the first sample. Exchange bias fields are displayed in Table 3.

Another interesting feature observed in the M vs. H measurements was the enhance of the coercive field observed in the FC mode with respect to the ZFC mode. The enhanced coercive field was also described in other nanoparticle AFM/F(i)M systems and is the result of the rotation through a spin drag effect of unpinned, uncompensated spins at the FM side of the interface[21,36]. In this case, not only the distinct occurrence of FeO is responsible for the measured H_C values, but also the nanoparticle size trend described before and its well-known relation with the blocking temperature and the H_C field can also explain part of this result.

Table 3: Coercive Fields and Exchange Bias Fields of the studied samples

Sample	Measure Mode	H_C (Oe)	H_E (Oe)
S1	FC	2100	1200
	ZFC	840	0
S2	FC	450	120
	ZFC	320	0
S3	FC	290	0
	ZFC	290	0
S6	FC	180	0
	ZFC	180	0

The ratio between the pinned and unpinned spins is known to be defined by the relationship of the AFM and FM anisotropies and the exchange coupling at the interface[21]. A dominant pinned state and the subsequent emergence of the exchange field requires a large AFM anisotropy compared to the FM anisotropy and the interface exchange constant. On the other hand, the opposite trend causes a larger population of unpinned spins and an enhancement of the coercive field during FC magnetization measurements. In our samples, the observation of both exchange field and enhanced coercivity at the FC measurements implies the existence of a population of both pinned and unpinned uncompensated spins at the interface. This suggests that there is no clear predominance by neither the AFM FeO anisotropy or the F(i)M Fe_3O_4 anisotropy and the interface exchange constant in the studied system.

Finally, the FC magnetization curves of the biphasic systems also show noticeable distorted symmetry and a small vertical shift of the hysteresis loop. Such behavior can be linked to the direction of the applied field during the measurement and how it defines the magnetization transitions as the cycle progresses[23,37]. For instance, in the direct process the Fe_3O_4 spins should only overcome their own anisotropy barrier to align with the magnetic applied field, but in the reversal process, i.e. when the field is antiparallel to the cooling field, they also need to overcome the exchange energy of the FeO phase at the interface.

4. Conclusions

In summary, we have studied a series of iron oxide nanoparticles prepared via thermal decomposition procedure. Different synthesis

conditions, such as gas atmosphere, precursor's ratio and heating rate were tested, and the nanoparticles were characterized by different techniques in order to understand the influence of the synthesis parameters on the final structure. We focused the discussion on the synthesis conditions that lead to the formation of bi-phasic core-shell $FeO@Fe_3O_4$ nanoparticles instead of the pure spinel systems. We found that the FeO phase is formed only in nanoparticles of around 16 nm of mean size, probably because the larger inner-particle diffusion length avoids the possibility to trigger a complete oxidation to Fe_3O_4 during the reaction time. Both, the FeO Néel transition temperature and the exchange coupling phenomenon were observed during the magnetic characterization of the $FeO@Fe_3O_4$ systems. The relative fraction of the iron oxide phases determines the magnitude and characteristics of the observed magnetic behaviors, with a more pronounced exchange phenomenon in the system with a larger yield of FeO.

Acknowledgements

Conflicts of interest

There are no conflicts of interest to declare.

References

1 S. Laurent, D. Forge, M. Port, A. Roch, C. Robic, L.V. Elst, R.N. Muller, Chem. Rev., 108 (2008) 2064–2110.

2 M. Knobel, W.C. Nunes, L.M. Socolovsky, E.D. Biasi, J.M. Vargas, J.C. Denardin, Journal of Nanoscience and Nanotechnology, 8 (2008) 2836–2857.

3 I. Koh, L. Josephson, Sensors, 9 (2009) 8130-8145.

4 Q.A. Pankhurst, J. Connolly, S.K. Jones, J. Dobson, J. Phys. D: Appl. Phys., 36 (2003) R167–R181.

5 L. Harivardhan Reddy, J.L. Arias, J. Nicolas, P. Couvreur, Chem. Rev., 112 (2012) 5818-5878.

6 S. Sun, H. Zeng, J. Am. Chem. Soc., 124 (2002) 8204-8205.

7 F. Vereda, J. de Vicente, R. Hidalgo-Alvarez, J. Colloid Interface Sci., 392 (2013) 50-56.

8 L. Vayssieres, C. Chaneac, E. Tronc, J.P. Jolivet, J. of Colloid Interface Sci., 205 (1998).

9 H. Iida, K. Takayanagi, T. Nakanishi, T. Osaka, J Colloid Interface Sci, 314 (2007) 274-280.

10 G. Salazar-Alvarez, J. Qin, V. Sepelak, I. Bergmann, M. Vasilakaki, K.N. Trohidou, J.D. Ardisson, W.A.A. Macedo, M. Mikhaylova, M. Muhammed, M.D. Baro, J. Nogués, J. Am. Chem. Soc., 130 (2008) 13234–13239.

11 C. de Montferrand, L. Hu, I. Milosevic, V. Russier, D. Bonnin, L. Motte, A. Brioude, Y. Lalatonne, Acta biomater., 9 (2013) 6150-6157.

12 J. Park, K. An, Y. Hwang, J.G. Park, H.J. Noh, J.Y. Kim, J.H. Park, N.M. Hwang, T. Hyeon, Nature materials, 3 (2004) 891-895.

13 C.J. Chen, H.Y. Lai, C.C. Lin, J.S. Wang, R.K. Chiang, Nanoscale Res. Lett., 4 (2009) 1343-1350.

14 I.-M. Grabs, C. Bradtmöller, D. Menzel, G. Garnweitner, Cryst. Growth Des., 12 (2012) 1469-1475.

15 H. Yun, X. Liu, T. Paik, D. Palanisamy, J. Kim, W.D. Vogel, A.J. Viescas, J. Chen, G.C. Papaefthymiou, J.M. Kikkawa, M.G. Allen, C.B. Murray, ACS nano, 8 (2014) 12323-12337.

16 H.T. Hai, H.T. Yang, H. Kura, D. Hasegawa, Y. Ogata, M. Takahashi, T. Ogawa, J. Colloid Interface Sci., 346 (2010) 37-42.

17 E. Wetterskog, C.-W. Tai, J. Grins, L. Bergström, G. Salazar-Alvarez, ACS nano, 7 (2013) 7132-7144.

18 Y. Hou, Z. Xu, S. Sun, Angew. Chem., 46 (2007) 6329-6332.

19 B.P. Pichon, O. Gerber, C. Lefevre, I. Florea, S. Fleutot, W. Baaziz, M. Pauly, M. Ohlmann, C. Ulhaq, O. Ersen, V.r. Pierron-Bohnes, P. Panissod, M. Drillon, S. Begin-Colin, Chem. Mater., 23 (2011) 2886-2900.

20 C.-J. Chen, R.-K. Chiang, H.-Y. Lai, C.-R. Lin, J. Phys. Chem. C, 114 (2010) 4258–4263.

21 D.W. Kavich, J.H. Dickerson, S.V. Mahajan, S.A. Hasan, J.H. Park, Phys. Rev. B, 78 (2008).

22 M. Estrader, A. Lopez-Ortega, I.V. Golosovsky, S. Estrade, A.G. Roca, G. Salazar-Alvarez, L. Lopez-Conesa, D. Tobia, E. Winkler, J.D. Ardisson, W.A. Macedo, A. Morphis, M. Vasilakaki, K.N. Trohidou, A. Gukasov, I. Mirebeau, O.L. Makarova, R.D. Zysler, F. Peiro, M.D. Baro, L. Bergstrom, J. Nogues, Nanoscale, 7 (2015) 3002-3015.

23 A. Lak, M. Kraken, F. Ludwig, A. Kornowski, D. Eberbeck, S. Sievers, F.J. Litterst, H. Weller, M. Schilling, Nanoscale, 5 (2013) 12286-12295.

24 S.K. Sharma, J.M. Vargas, K.R. Pirota, S. Kumar, C.G. Lee, M. Knobel, J. Alloy. Comp., 509 (2011) 6414-6417.

25 J. Nogués, J. Sort, V. Langlais, V. Skumryev, S. Suriñach, J.S. Muñoz, M.D. Baró, Physics Reports, 422 (2005) 65–117.

26 G.C. Lavorato, E. Lima, Jr., D. Tobia, D. Fiorani, H.E. Troiani, R.D. Zysler, E.L. Winkler, Nanotechnology, 25 (2014) 355704.

27 R. Cabreira-Gomes, F.G. Silva, R. Aquino, P. Bonville, F.A. Tourinho, R. Perzynski, J. Depeyrot, J. Magn. Magn. Mater., 368 (2014) 409-414.

28 M. Feygenson, J.C. Bauer, Z. Gai, C. Marques, M.C. Aronson, X. Teng, D. Su, V. Stanic, V.S. Urban, K.A. Beyer, S. Dai, Phys. Rev. B, 92 (2015).

29 S. Chandra, N.A. Huls, M.H. Phan, S. Srinath, M.A. Garcia, Y. Lee, C. Wang, S. Sun, O. Iglesias, H. Srikanth, Nanotechnology, 25 (2014) 055702.

30 M.S. Carrião, A.F. Bakuzis, Nanoscale, 8 (2016) 8363-8377.

31 H.L. Ding, Y.X. Zhang, S. Wang, J.M. Xu, S.C. Xu, G.H. Li, Chem. Mater., 24 (2012) 4572-4580.

32 M. Lattuada, T.A. Hatton, Langmuir, 23 (2007) 2158-2163.

ARTICLE

Journal Name

33 L.A. Feigin, D.I. Svergun, Structure Analysis by Small-Angle X-Ray and Neutron Scattering, New York: Plenum Press, 1989.

34 L.M. Socolovsky, O. Moscoso-Londoño, Consequences of Magnetic Interactions Phenomena in Granular Systems, in: S.K. Sharma (Ed.) Complex Magnetic Nanostructures - Synthesis, Assembly and Applications, Springer, Rio de Janeiro, 2017.

35 O. Moscoso-Londoño, P. Tancredi, D. Muraca, P. Mendoza Zélis, D. Coral, M.B. Fernández van Raap, U. Wolff, V. Neu, C. Damm, C.L.P. de Oliveira, K.R. Pirota, M. Knobel, L.M. Socolovsky, J. Magn. Magn. Mater., 428 (2017) 105-118.

36 E. Lima, E.L. Winkler, D. Tobia, H.E. Troiani, R.D. Zysler, E. Agostinelli, D. Fiorani, Chem. Mater., 24 (2012) 512-516.

37 M.R. Fitzsimmons, P. Yashar, C. Leighton, I.K. Schuller, J. Nogués, C.F. Majkrzak, J.A. Dura, Phys. Rev. Lett., 84 (2000) 3986-3989.

New Journal of Chemistry Accepted Manuscript
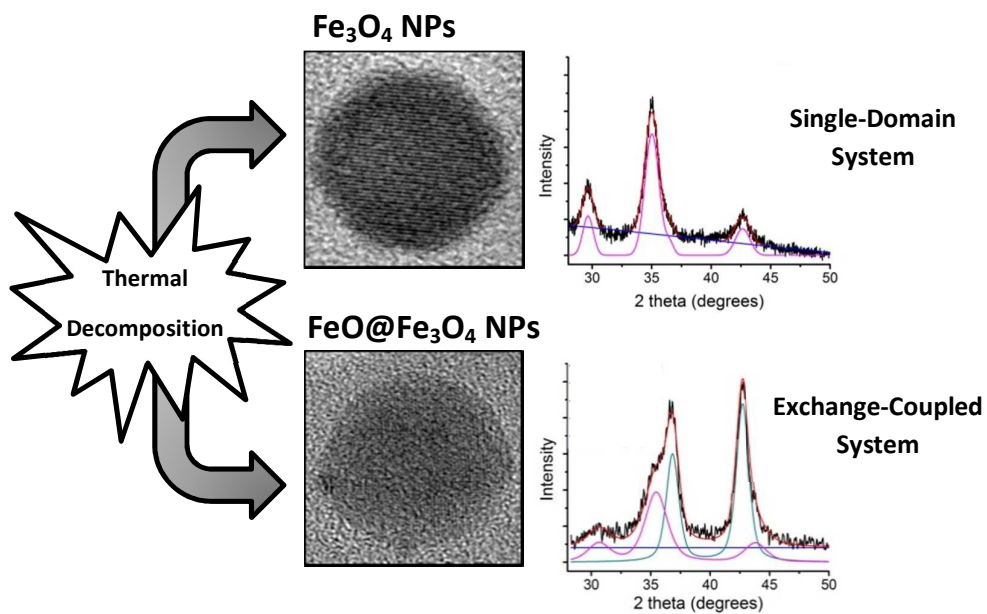
In this work we study the link between synthesis conditions, crystalline structure and magnetic properties of exchange-coupled and single-domain iron oxide nanoparticles